THE JOURNAL OF PHYSICAL CHEMISTRY C

pubs.acs.org/JPCC Article

Composition Effects on Ultrafast Optical Properties of Cu_xO_y Thin Films: A Transient Absorption Study

Learnmore Shenje, Steven Larson, Yiping Zhao,* and Susanne Ullrich*

Cite This: *J. Phys. Chem. C* 2020, 124, 24908−24918 Read Online

ACCESS | Metrics & More | Article Recommendations | Supporting Information

ABSTRACT: Cu_2O, CuO, and mixed-phase Cu_2O/CuO thin films with different relative compositions were prepared by oxidizing Cu films at temperatures 150−380 °C for a time period ranging from 2 to 24 h, and their ultrafast transient absorption spectra have been characterized to understand the carrier dynamics of the heterostructured Cu_2O/CuO system. The absorption dynamics of a pure p-type Cu_2O sample followed a biexponential decay, with a fast time ~0.3 ps and a long life >150 ps, while a pure p-type CuO sample showed triexponential decay dynamics, with three time constants, 0.25, 2.5, and >150 ps. For the mixed-phased Cu_2O/CuO thin films, their absorption dynamics all followed the triexponential decay, and the two ultrafast time constants showed strong composition dependence. Possible energy band structures and electron transition processes are proposed to understand both the spectroscopic and dynamics behaviors of these samples.

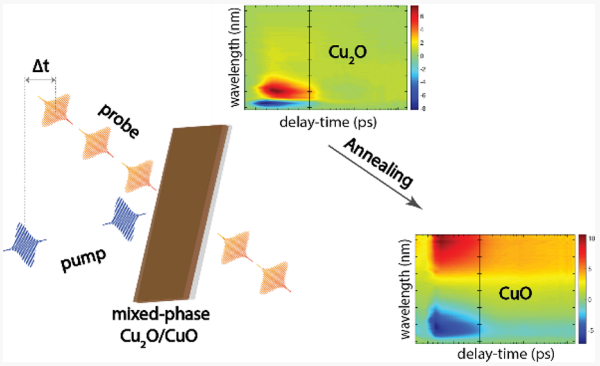

1. INTRODUCTION

Copper oxide is known to exist in three phases, Cu_2O (cuprite), CuO (tenorite), and Cu_4O_3 (paramelaconite).[1,2] These binary oxides are attractive candidates for optoelectronic applications, including photovoltaics, photocatalysis, and all-optical switching, primarily because of their favorable bandgaps. These materials are also inexpensive and environmentally benign.[1,3−5] Cu_2O (bandgap 1.9−2.6 eV), a natural p-type semiconductor, has extensively been studied for its excitonic behavior, but interest has recently shifted to potential solar cell applications.[6] CuO (bandgap 0.8−1.8 eV), also a p-type semiconductor,[7−10] has shown promise in catalytic, gas sensing, and magnetic applications. By varying deposition conditions, the bandgaps for Cu_2O and CuO can be tuned from 1.2 to 2.6 eV, making them versatile materials for solar absorption in photovoltaic devices.[1,11] In addition, due to favorable band edge misalignment that places the CuO valence band and conduction band lower than those of Cu_2O and the potential charge separation mechanism, heterostructured Cu_2O/CuO thin films or nanostructures have been proven to have better photocatalytic performance compared to Cu_2O or CuO single-component materials.[12−16] For example, Jiang et al. reported on CuO/Cu_2O nanowires with methyl orange (MO) degradation rates 260 times higher than pure Cu_2O.[15] These high reaction rates were mainly attributed to charge separation and transfer between the two oxide phases. Further applications in water photoelectrolysis have also been achieved by combining Cu_2O and CuO to form heterojunctions.[12] The enhanced photocatalytic performance for Cu_2O/CuO heterostructures is most likely determined by the change of photoinduced carrier dynamics and charge transfer in the material system.

To understand charge carrier processes of a semiconductor material, femtosecond transient absorption pump−probe spectroscopy (TAS) is commonly used as it provides powerful means to characterize charge carrier dynamics by monitoring pump-induced changes in the optical absorption spectrum across different probe wavelengths.[17−19] Photoexcitation across the semiconductor bandgap is of particular interest; in this case, the pump photon energy is transferred to these carriers via interband transitions. As the system evolves back to equilibrium, electron (hole) relaxation in the conduction band (valence band) via carrier−carrier or carrier−phonon interactions occurs on a femtosecond time scale.[17−19] Subsequently, these carriers can recombine radiatively or nonradiatively from the bottom of the conduction band and the top of the valence band. In the presence of midgap states (defect and/or surface states), carrier trapping can also provide another relaxation pathway on the tens-of-picoseconds to hundreds-of-picoseconds time scale.[19] In the pump−probe optical absorption spectrum, the ground-state population is monitored as a transient bleach signal indicating the initial depletion and

Received: September 24, 2020
Revised: October 18, 2020
Published: October 30, 2020

https://dx.doi.org/10.1021/acs.jpcc.0c08716
J. Phys. Chem. C 2020, 124, 24908−24918

subsequent recovery of the ground-state population after undergoing momentum and energy relaxation, whereas free and trapped carriers are typically represented by rising or decaying absorptive signals.[18,19] In addition to interband transitions, excitations from lower to higher levels of the valence band may also contribute and equilibrate via carrier−carrier or carrier−phonon scattering.[5] The carrier dynamics of many conventional oxide materials such as TiO_2,[20−2220−22] Fe_2O_3,[23,2423,24] and ZnO[21,25] have been studied extensively based on TAS. However, there are only a few studies that have investigated the carrier dynamics of CuO and Cu_2O. Othonos and Zervos showed that for CuO nanowires, the fast dynamics of the photoinduced carriers followed a double exponential decay with time constants of 0.4 and 2.1 ps.[26] Born et al. reported that for CuO nanocrystals deposited on a glass substrate, there existed three time constants:[27] the smallest time constant was around 330 to 630 fs, which was attributed to momentum relaxation via carrier−carrier scattering in the valence band as well as exciton−exciton annihilation; the second time constant was at 2 ps due to energy relaxation via carrier−phonon scattering within the valence band; and the third time constant, 50 ps, was associated with trapping and recombination of the high density of trap states within the CuO nanocrystals. Azimi et al. investigated the TAS of Cu_2O nanoparticles and discovered that the TA signal followed a biexponential decay, with an ultrafast decay time ∼0.5 ps and a long life component >8 ns.[28] They attributed the small decay time to the underlying excitonic state, while the long time was due to defects/trap states. Studies by optical-pump THz-probe spectroscopy showed that the minority carrier lifetime of Cu_2O thin films deposited by electrodeposition was 140−180 ps.[29] The dynamics of incoherent exciton formation under interband photoexcitation in a Cu_2O crystal was investigated by Tanimura et al. using time- and angle-resolved photoemission spectroscopy at 90 K.[30] A very recent study on the carrier relaxation of Pt-covered Cu_2O by femtosecond time-resolved two-photon photoemission yielded two time constants, a rapid time constant on the order of 1 ps and a slower time constant in the range of 80 ps.[31] However, the above reported carrier dynamics were determined from different kinds of samples with different ultrafast spectroscopy techniques. Gaining a coherent understanding of the carrier dynamics of CuO, Cu_2O, and their heterostructures necessitates ultrafast spectroscopy measurements on samples from the same preparation method and with systematic changes of the relative composition.

One well-known CuO and Cu_2O sample preparation technique is a two-step thin-film processing method. Cu thin films are deposited through conventional physical vapor deposition and subsequently oxidized in an oxygen-rich environment at different temperatures and time duration to produce different oxides or mixture-phased thin films.[3,32,33] Khojier et al. and Brown et al. separately showed that Cu oxidation to Cu_2O and CuO in thin films was directly related to annealing temperature, time, and environment.[3,32] Below 250 °C, samples composed of Cu_2O were obtained but 350 to 400 °C annealing resulted in the CuO phase. Intermediate temperatures gave rise to a mixture of the two oxide phases. Basnet et al. reported on temperature-dependent oxidation of Cu_2O nanorods to CuO.[34] Their results show a systematic decrease in effective bandgap with increasing annealing temperature, which they attributed to the change of phase.[34]

In the present study, the charge carrier dynamics in Cu_2O, CuO, and mixed-phase Cu_2O/CuO thin films prepared by Cu film oxidations are studied systematically by TAS. Sample phase compositions and bandgaps are determined by X-ray diffraction (XRD) and UV−vis, respectively.

2. METHODS

The CuO, Cu_2O, and Cu_2O/CuO mixed-phase thin films were prepared by oxidation of Cu thin films at different conditions, according to ref 34. Glass slides of 1 cm × 1 cm were cleaned by boiling in a mixture of 4:1 (volume ratio) concentrated H_2SO_4 (Fisher Scientific, 98%) and 30% H_2O_2 (Fisher Scientific, 98%) for 20 min. Samples were then rinsed with 18 MΩ deionized (DI) water, dried under a flow of nitrogen gas, and then loaded into a custom-built electron beam deposition chamber. The deposition system was then pumped down to a background pressure of less than 1×10^{-6} Torr. During the deposition, the evaporation rate of Cu (Alfa Aesar, 99.99%) was set to be 0.1 nm/s until a final thickness of 100 nm was reached. Both the film thickness and deposition rate were monitored by a quartz crystal microbalance and the chamber pressure was kept below 1×10^{-4} Torr. After deposition, the samples were allowed to cool to room temperature in vacuum. The as-deposited Cu thin films were oxidized for a time duration of 2, 4, 8, or 24 h at a temperature of 150, 200, 290, or 380 °C, respectively, in a quartz tube furnace (Lindberg/Blue 5.1 KW, Model:HFT553476) under a 20 sccm flow of ultra-high-purity oxygen gas (99.994% AirGas OX-UHP) after ramping from room temperature at a rate of 5 °C/min. The treated thin-film samples from this point on will be referenced by their annealing time (superscript) and temperature (subscript) with the letter C as short for copper oxide. For example, samples annealed at 150 °C for 4 h will be labeled as $^4C_{150}$.

The crystal structures of the samples were characterized by a PANalytical X'Pert PRO MRD X-ray diffractometer with a fixed incidence angle of 0.5°. The XRD patterns were recorded with Cu Kα_1 radiation (λ = 1.5405980 Å). The composition of each sample was estimated by the Rietveld refinement method using PANalytical X'Pert HighScore Plus. Steady-state UV/Vis data was recorded by a commercially available Jasco V-570 UV/Vis/NIR spectrophotometer.

The setup for transient absorption measurements is based on a commercially available 1 kHz regenerative amplifier (Coherent Inc Legend Elite seeded by a Mira Optima 900) and custom-built transient absorption spectrometer.[35] Approximately, 600 mW of the 800 nm fundamental with a temporal width of 130 fs was used for the experiments. Four hundred and eighty megawatts was frequency-doubled in a β barium borate crystal to generate 1.5 mW of 400 nm (3.1 eV) excitation pulses. To gain access to visible pump wavelengths, another part of the Legend output was used to pump a traveling wave optical parametric amplifier (TOPAS-C). An optical chopper (Thorlabs MC2000) operating at 500 Hz was used to block every other pump pulse before it was focused with a 750 mm focal length lens onto the sample position. The remaining 120 mW of the fundamental was passed through a neutral density filter and focused into a 3 mm sapphire crystal to generate a white-light continuum (WLC) probe beam ranging from 440 to 800 nm. The transmitted WLC spectrum was then recorded with a fiber spectrometer (AvaSpec-1650F-USB2) and the transient absorption (TA) data was computed as the difference in optical density with pump on and off. The

https://dx.doi.org/10.1021/acs.jpcc.0c08716
J. Phys. Chem. C 2020, 124, 24908−24918

time evolution of the TA spectrum was obtained by means of a variable optical delay between the pump and probe pulses. The latter was facilitated by a retroreflector mounted on a computer-controlled linear translation stage (Newport Inc, ILS150PP with an ESP 301 controller) within the probe beam path. All experiments were carried out at room temperature. Surface Xplorer and Glotaran packages were used for data preprocessing and global fitting, respectively.[36,37]

3. RESULTS AND DISCUSSION

3.1. X-ray Diffraction. Figure 1 shows the XRD patterns of six representative samples, $^{2}C_{150}$, $^{4}C_{150}$, $^{24}C_{150}$, $^{2}C_{200}$, $^{2}C_{380}$, and $^{24}C_{380}$, annealed for different times (t) and at different temperatures (T), respectively, and their visual appearances are shown in Figure S1 of the Supporting Information (SI). Clearly with increased time or elevated oxidation temperature, the crystalline structures of the thin films change significantly. In particular, the XRD patterns of $^{2}C_{150}$ and $^{24}C_{380}$ are distinctly different: the $^{2}C_{150}$ only shows individual crystalline peak positions for Cu_2O (solid squares), while the $^{24}C_{380}$ only demonstrates the diffraction peaks for CuO (solid triangles). At the low oxidation temperature (T = 150 °C), with an increase of t, the XRD patterns are dominated by the Cu_2O crystal phase. However, the crystal phase of the samples is very sensitive to oxidation temperature. Comparing XRD patterns of the $^{2}C_{150}$, $^{2}C_{200}$, and $^{2}C_{380}$ samples, prominent $Cu_2O(111)$ and (200) peaks in $^{2}C_{150}$ decrease in intensity when T increases from 150 to 200 °C and then almost disappear, while the CuO(111) and (11$\bar{1}$) peaks start to show up at T = 380 °C. This result indicates a shift of the Cu_2O crystal phase to a CuO crystal phase and the formation of a mixed Cu_2O and CuO sample. At T = 380 °C and increasing t from 2 h ($^{2}C_{380}$) to 24 h ($^{24}C_{380}$), the CuO(111) and (11$\bar{1}$) peaks become sharper and more distinct and other XRD peaks for crystalline CuO appear, which indicates that the quality of the CuO crystalline structure of the thin film improves significantly. The relative Cu_2O and CuO composition ratios η_{Cu_2O} and η_{CuO} were determined by the Rietveld refinement method from the XRD patterns and are summarized in Table 1 for different oxidized samples. The Rietveld refinement method is a reliable way to determine crystallite phase compositions and has been used for Cu_2O/CuO nanorods and other materials.[34,38,39] The $^{2}C_{150}$ sample has almost 99% Cu_2O, whereas the $^{24}C_{380}$ sample has 1.2% Cu_2O (i.e., 98.8% CuO). The small amount of Cu_2O in the $^{24}C_{380}$ sample indicates that there could be excessive copper ions compared to the stoichiometry of intrinsic CuO, indicating the existence of many defect states in the sample. With the increase of t and T, the relative ratio of CuO to Cu_2O increases, as shown in Table 1.

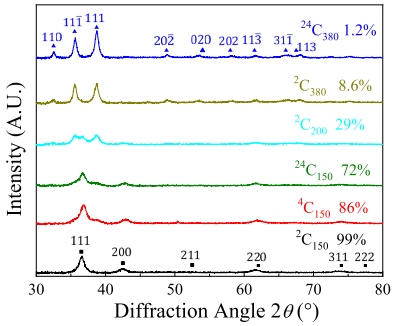

Figure 1. XRD patterns of the different CuO/Cu_2O thin-film samples. The black squares mark the characteristic peaks for Cu_2O (JCPDS ref no. 078-2076) and the blue triangles label the peaks from CuO (JCPDS ref no. 048-1548). The percentage refers to the relative Cu_2O composition determined by the Rietveld refinement method.

Table 1. Relative Compositions of the Cu_2O and CuO in the Oxidized Cu Thin Films at Different Conditions Determined by the Rietveld Method

	composition	
sample name	η_{Cu_2O}	η_{CuO}
$^{2}C_{150}$	99	1
$^{4}C_{150}$	86	14
$^{24}C_{150}$	72	28
$^{2}C_{200}$	29	71
$^{2}C_{380}$	8.6	91.4
$^{24}C_{380}$	1.2	98.8

3.2. Steady-State UV/Visible Absorption. The optical extinction spectrum $e(h\nu)$ of any sample is determined by

$$e(h\nu) = -\ln T_0(h\nu) \quad (1)$$

where $T_0(h\nu)$ is the transmission spectrum, h is Planck's constant, and ν is the photon's frequency. Since the samples studied were very thin and had small and constant reflectance in the wavelength range considered here (see Section S2 of the SI), we assume that $e(h\nu)$ equals to the optical absorption spectrum, i.e., $e(h\nu) \approx \alpha(h\nu)d$, where $\alpha(h\nu)$ is the absorption coefficient and d is the oxide film thickness, which is known from the deposition. For the $^{2}C_{150}$ sample, we assume that it is a pure Cu_2O reference sample, its $e^{Cu_2O}(h\nu) \approx \alpha^{Cu_2O}(h\nu)d$, and the $^{24}C_{380}$ represents a pure CuO sample, so $e^{CuO}(h\nu) \approx \alpha^{CuO}(h\nu)d$. Here, the superscript denotes the type of the copper oxide. Figure 2a plots the measured $e^{Cu_2O}(h\nu)$ and $e^{CuO}(h\nu)$ on a semilog scale for samples $^{2}C_{150}$ and $^{24}C_{380}$. Both spectra show similar trends: at small photon energy, there is little extinction, while for $\nu > \nu_c$ (a critical frequency), the $e(h\nu)$ increases significantly with the increase of ν, where ν_c is related to the effective optical bandgap (OBG) E_g of the material. The E_g can be extracted from a Tauc plot according to the following equation,[40]

$$[\alpha(h\nu)h\nu]^{1/n} = A(h\nu - E_g) \quad (2)$$

where A is a proportionality constant, n = 1/2 for direct band transitions, and n = 2 for indirect band transitions. The Tauc plots for samples $^{2}C_{150}$ and $^{24}C_{380}$ are shown in Figure S4a,b and the resulting direct (indirect) OBGs are extracted as $E_D^{Cu_2O}$ = 2.48 eV ($E_i^{Cu_2O}$ = 1.55 eV) for $^{2}C_{150}$ and E_D^{CuO} = 2.20 eV (E_i^{CuO} = 1.05 eV) for $^{24}C_{380}$, which are in general agreement with the values reported in the literature. Both Cu_2O and CuO are reported to have a direct OBG ranging from 2.1−2.6 to 1.3−3.0 eV and an indirect OBG of 2.1−2.21 and 1.2−2.1 eV, respectively.[27,32,34] The lower indirect OBGs observed here as compared to literature values can be attributed to differences in sample deposition techniques and annealing conditions.[34] In addition, since there are still impurities in both $^{2}C_{150}$ and $^{24}C_{380}$ samples, there exists a significant number of defects close to the energy band edge. These defect states are characterized by Urbach's tail in optical absorption spectroscopy[27,41]

$$\alpha(h\nu) = \alpha_0 \, e^{\sigma(h\nu - E_U/k_B T_R)} \quad (3)$$

https://dx.doi.org/10.1021/acs.jpcc.0c08716
J. Phys. Chem. C 2020, 124, 24908−24918

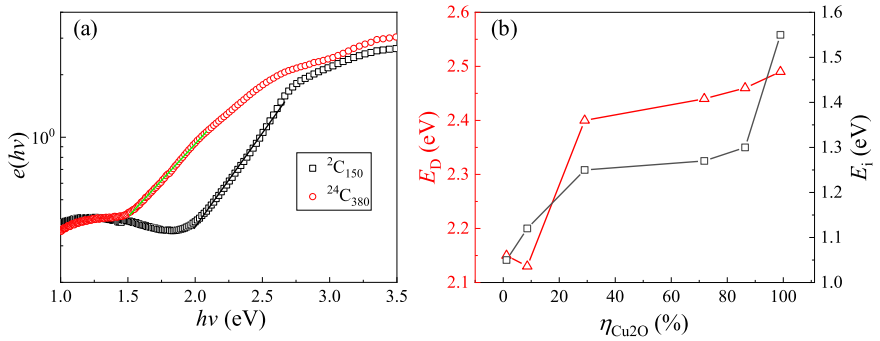

Figure 2. (a) Semilog plots of the extinction spectra $e(h\nu)$ versus $h\nu$ for samples $^2C_{150}$ (η_{Cu_2O} = 99%) and $^{24}C_{380}$ (η_{Cu_2O} = 1.2%) and (b) plots of the direct (red triangles) and indirect (black squares) bandgap determined by Tauc plots versus the composition of Cu_2O (η_{Cu_2O}) in the samples.

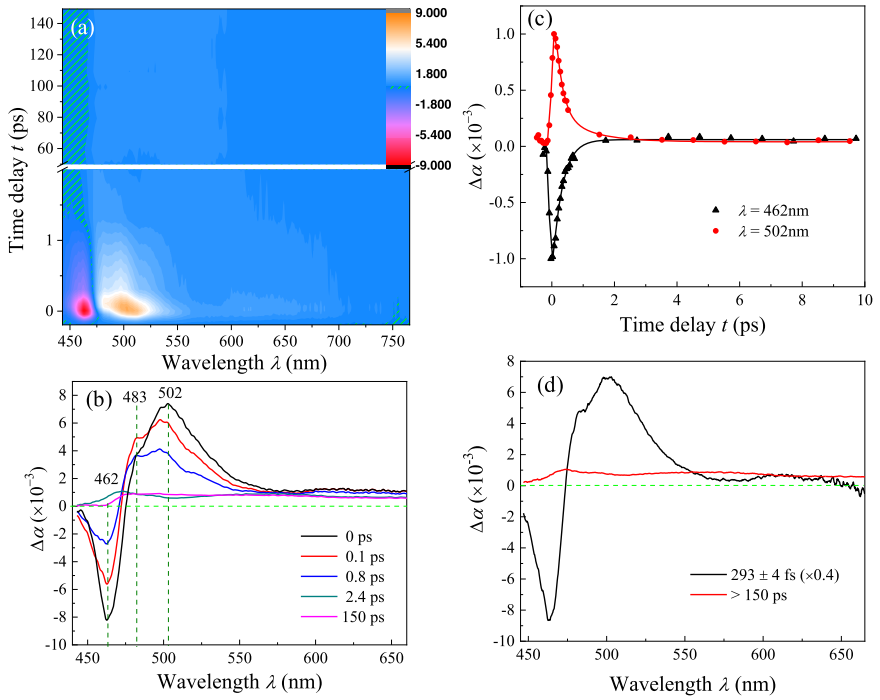

Figure 3. Chirp-corrected TA spectra of sample $^2C_{150}$ (η_{Cu_2O} = 99%): (a) Overall two-dimensional (2D) TA map. (b) Representative TA spectra at delay time t = 0, 0.1, 0.8, 2.4, and 150 ps. (c) Representative time-dependent TA curves at two characteristic wavelengths, the bleach dip λ_b = 462 nm and the induced resonance absorption peak λ_p = 502 nm. The solid curves are fitting results based on a sequential biexponential model. (d) Plots of the resulting evolution associated spectra (EAS) for $T_1^{Cu_2O}$ = 293 fs and $T_2^{Cu_2O} \geq$ 150 ps based on the global analysis technique.

where E_U and α_0 are the characteristic parameters of Urbach's tail of the material, σ is the steepness parameter, k_B is the Boltzmann constant, and T_R is the room temperature. As shown in Figure 2a, the linear fit in the semilog plots gives $E_U^{Cu_2O}$ = 2.48 eV and E_U^{CuO} = 2.05 eV, which, according to eq 3, correspond to the photon energy where $e(h\nu) = 10^0$. Therefore, both reference samples, $^2C_{150}$ and $^{24}C_{380}$, have significant defects that could affect their optical absorption and will eventually influence the photocarrier dynamics.

For a mixed-phase Cu_2O/CuO thin film, though an effective medium theory could be used to predict the overall extinction or absorption spectra of the films based on those of the samples $^2C_{150}$ and $^{24}C_{380}$ and the relative composition ratio of Cu_2O/CuO, the relationship would become very complicated. Here, based on the overall extinction or absorption of the mixed-phase thin film, a simple linear model can be assumed for the extinction spectrum only based on the composition,

$$e^{mix}(h\nu) \approx [\alpha^{Cu_2O}(h\nu)\eta_{Cu_2O} + \alpha^{CuO}(h\nu)\eta_{CuO}]d \quad (4)$$

Figure S5 shows an example of the $e^{mix}(h\nu)$ for sample $^{24}C_{150}$ and the calculated extinction spectrum based on eq 4, the spectra of $^2C_{150}$ and $^{24}C_{380}$, and the composition ratio in Table 1. Despite some discrepancies at high photon energy $h\nu$, the measured $e^{mix}(h\nu)$ and calculated $e^{mix}(h\nu)$ agree fairly well, which means that eq 4 could be used roughly to predict the general trend for $e^{mix}(h\nu)$. Both eq 4 and Section S3 in the SI indicate that the mixed-phase thin films do not have an intrinsic optical bandgap, and the effective bandgap is a complex function of the composition. Figure S4 shows the corresponding Tauc plots, and the corresponding effective $E_D^{Cu_2O}$ and $E_i^{Cu_2O}$ versus η_{Cu_2O} are plotted in Figure 2b. A significant increase in both $E_D^{Cu_2O}$ and $E_i^{Cu_2O}$ is observed with the increase of η_{Cu_2O}, which is consistent with the reports in the literature.[3,34]

https://dx.doi.org/10.1021/acs.jpcc.0c08716
J. Phys. Chem. C 2020, 124, 24908−24918

3.3. TA Spectra of the Reference Cu_2O Thin Film. The time- and wavelength-dependent TA spectra $\Delta\alpha^{Cu_2O}(\lambda,t)$ of the $^2C_{150}$ sample (i.e., the pure Cu_2O reference sample) is shown in Figure 3a, and two unique spectra−time regions are visible: a dip (bleach) area at delay time region $0 < t < 0.5$ ps and spectral region $450 < \lambda < 475$ nm and an induced absorption area at a similar delay time region but a longer-wavelength region $475 < \lambda < 525$ nm. Figure 3b shows the corresponding TA spectra $\Delta\alpha^{Cu_2O}(\lambda,t)$ at selective delay times, t = 0, 0.1, 0.8, 2.4, and 150 ps. The early time ($t < 1$ ps) spectra show two distinct features: a sharp bleach between 445 and 475 nm with a dip at λ_b = 462 nm ($h\nu_b$ = 2.68 eV) and an induced absorption peak in the wavelength region 475−550 nm, with a major peak, which blue shifts slightly (λ_p = 503 nm ($h\nu_p$ = 2.46 eV) at t = 0 ps to λ_p = 497 nm at t = 0.8 ps) with time and a shoulder (λ_s = 483 nm ($h\nu_s$ = 2.57 eV)) that stays almost unchanged. When $t \geq 2.4$ ps, the bleach is totally recovered and there is are broad induced absorption features extended from λ = 460 to 700 nm. These time-dependent spectral features indicate that the bleach and induced absorption occur simultaneously and are both directly linked to the pump beam or the photocarrier generation; both the bleach dip and absorption peak decay as a function of time; when $t > 2.4$ ps, the featureless broad absorption band, which extends to the longer-wavelength region, indicates intraband transitions.

Using the global lifetime analysis (see details in Section S4 of the SI), the time-dependent TAS data for the Cu_2O sample can be fully described by a biexponential model convoluted with a Gaussian function. Figure 3c shows two representative $\Delta\alpha$ versus t curves at λ_b = 462 nm (the bleach dip at 462 nm) and λ_p = 503 nm (the induced absorption peak). Both curves are fitted with two global time constants, $T_1^{Cu_2O}$ = 293 fs and $T_2^{Cu_2O} \geq 150$ ps. Based on the fitting, the resulting evolution associated spectra (EAS) for $T_1^{Cu_2O}$ = 293 fs and $T_2^{Cu_2O} \geq 150$ ps are obtained and plotted in Figure 3d. The results are very similar to what was reported by Azimi et al., who obtained $T_1^{Cu_2O}$ = 0.5 ps and $T_2^{Cu_2O} \geq 8$ ns for Cu_2O nanoparticles, and attributed $T_1^{Cu_2O}$ as the lifetime of the excitons.[28] The electron process associated with the long lifetime $T_2^{Cu_2O}$ in the order of 10^{-10} s, could be due to the defect trapping (see the green arrow between the CB and defect state of Figure 4). This value is similar to the hole lifetime of Cu_2O thin films observed by Paracchino et al. using the optical-pump THz-probe spectroscopy,[29] which suggests that the hole dynamics could play a role here. The EAS for $T_1^{Cu_2O}$ manifests similarities to $\Delta\alpha(\lambda, t = 0)$, showing two spectral characteristics in Figure 3a, the bleach dip and the induced absorption peak, while the EAS for $T_2^{Cu_2O}$ is a broad featureless spectrum.

According to the literature, a bleach signal is typically due to the depletion of the valence electrons, although the bleach dip location is at higher energy with respect to the bandgap because the transient spectrum is the first derivative of the ground-state absorption spectrum.[42] In fact, as shown in Figure S6a, the bleach peak location for Cu_2O is at 2.68 eV, which is close to the dip location at 2.63 eV of the first derivative of the UV−vis absorption spectrum.[42] This feature can be attributed to absorption to higher conduction band states and is consistent with experimentally observed transitions in Cu_2O using spectroscopic ellipsometry by Meyer et al.[43,44] The induced absorption centers around $h\nu_p$ = 2.46 eV, which could be due to several reasons (see Figure 4): the electrons in the Γ_8^- conduction band could further absorb probe photons to be excited into higher conduction bands (the red arrow in CB of Figure 4) or the electrons from the deep valent bands can recombine with a high concentration of holes in the Γ_7^+ valance band (the red arrow in VB of Figure 4). Both situations, in principle, could occur due to the complex band structure of Cu_2O.

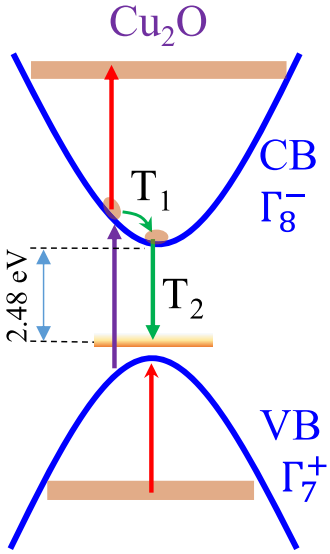

Figure 4. Proposed energy band structures and possible electron transition processes for the p-type Cu_2O thin film.

The early time carrier dynamics depend on the excited carrier population N. For the bleach that occurs at $h\nu_b$ = 2.68 eV, the pump-induced optical absorption,

$$\Delta\alpha^{Cu_2O}(h\nu_b) = -\frac{\alpha^{Cu_2O}(h\nu_b)N}{N + N_{sat}} \quad (5)$$

where N_{sat} is a saturation electron density in the VB. Under the assumption that $N \ll N_{sat}$, eq 5 reduces to, $\frac{\Delta\alpha^{Cu_2O}}{\alpha^{Cu_2O}} = -\frac{N}{N_{sat}}$, i.e., the induced absorption peak shares the same time constant $T_1^{Cu_2O}$ as that for the bleach dip. According to literature, $T_1^{Cu_2O}$ could be due to electronic dephasing, which is in the order of tens to hundreds fs, and the intraband relaxation, in the same order of time frame (see the green arrow in CB of Figure 4).[12,45] Phenomenologically, the induced absorption peak can be fitted by the following Gaussian-like function,

$$\Delta\alpha^{Cu_2O}(h\nu) = \sigma_p N\, e^{(h\nu - E_p/\Delta E)^2} \quad (6)$$

where σ_p is the induced absorption cross section, E_p is the absorption peak location, and ΔE is the spectral width. Based on the absorption peak in Figure 3b, one obtains $\sigma_p N(t = 0)$ = 5.39 ± 0.04, E_p = 2.46 ± 0.01 eV, and ΔE = 0.113 ± 0.001 eV.

The broad featureless spectrum EAS for $T_2^{Cu_2O}$ indicates the occurrence of multiple induced absorptions. When $t > T_1^{Cu_2O}$, the pump-induced excessive electrons not only populate the CB but also trap states. Therefore, hot carrier-induced absorption, intraband absorption from the edge of the CB to high-energy levels of the CB, as well as the defect absorption would occur, which contributes to the broadness of the EAS.

3.4. TA Spectra of the Reference CuO Thin Film. The time- and wavelength-dependent TA spectra $\Delta\alpha^{CuO}(\lambda,t)$ of the $^{24}C_{380}$ sample (i.e., the pure CuO reference sample) is shown in Figure 5a. Two unique spectra−time regions are observed: a

https://dx.doi.org/10.1021/acs.jpcc.0c08716
J. Phys. Chem. C 2020, 124, 24908−24918

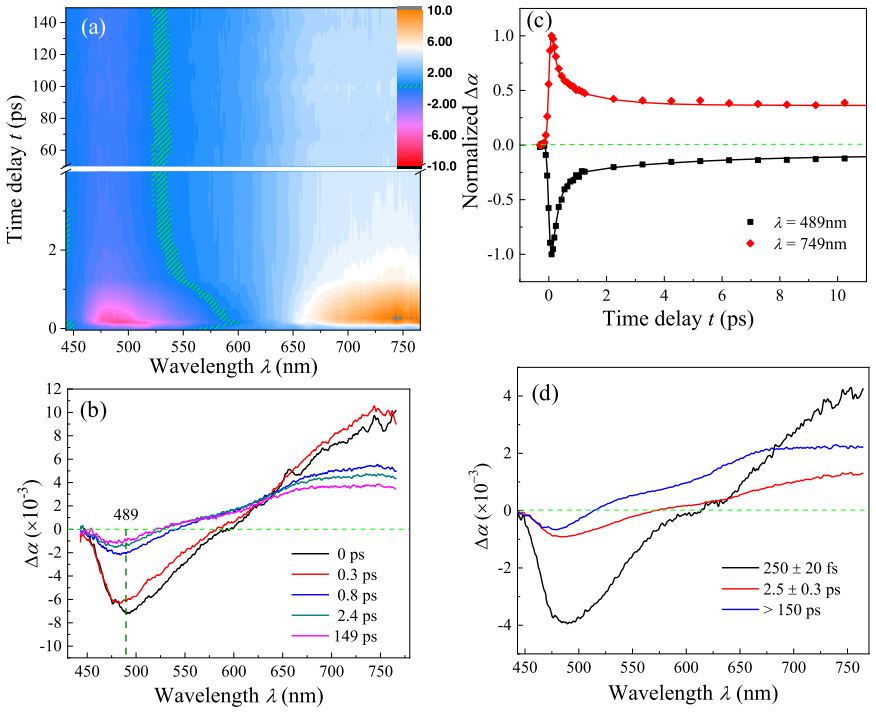

Figure 5. Chirp-corrected TA spectra of sample $^{24}C_{380}$ (η_{Cu_2O} = 1.2%): (a) Overall 2D TA map. (b) Representative TA spectra at delay time t = 0, 0.3, 0.8, 2.4, and 150 ps. (c) Representative time-dependent TA curves at two characteristic wavelengths, the bleach dip λ_b = 489 nm and the free carrier absorption (FCA) λ_0 = 749 nm. The solid curves are fitting results based on a triexponential decay function. (d) Plots of the corresponding evolution associated spectra.

dip (bleach) area at a delay time $0 < t < 1$ ps and spectral region $450 < \lambda < 650$ nm and an induced absorption area at a delay time region $0 < t < 2$ ps and a longer-wavelength region $\lambda > 650$ nm. Compared to the corresponding map for Cu_2O samples, the bleach spectral features become broader and the spectral peak width decreases with delay time. For the pump-induced absorption, the spectral region redshifts significantly to the near IR region. Figure 5b shows the corresponding TA spectra $\Delta\alpha^{CuO}(\lambda,t)$ at selective delay times, t = 0, 0.3, 0.8, 2.4, and 149 ps. Regardless of the delay time, all spectra show similar features: a broad bleach dip centered at λ_b = 490 nm ($E_b^{CuO} = h\nu_b$ = 2.53 eV) and a broad absorption feature at a larger wavelength. The dip energy is also significantly larger than E_D^{CuO} = 2.20 eV.

Based on eq 7, we can also obtain that $\frac{N'}{N'_{sat}} \approx 5.4 \times 10^{-3}$, i.e., the free carrier generation ratios for CuO and Cu_2O in our experiments are about the same. With an increase in t, the bleach dip slightly blue shifts, its magnitude decreases but does not diminish within the time scale of our measurements. The overall absorption at longer wavelengths also decreases with t. Furthermore, the absorptive signal shows a monotonic increase in intensity with wavelength λ. Such a $\Delta\alpha^{CuO}(\lambda,t)-\lambda$ relationship is a characteristic of free carrier absorption (FCA),[46,47] which can be fitted by the empirical equation,

$$\Delta\alpha^{CuO}(h\nu) = A_0 + \sum_{i=1}^{3} A_i(\lambda - \lambda_0)^{p_i} \quad (7)$$

where p_1 = 1.5 is attributed to the scattering by the acoustic phonons; p_2 = 2.5 for the scattering by the optical phonons; and p_3 = 3.5 for the scattering by ionized impurities.[47] A_i (i = 0, 1, 2, and 3) are the corresponding coefficient. Figure S7a,b shows the fitting results for $\Delta\alpha^{CuO}(\lambda,t)(\lambda,t$ = 0.7 ps) and $\Delta\alpha^{CuO}(\lambda,t)(\lambda,t$ = 85.4 ps). This result is consistent with the report by Wang et al.,[48] where the transient absorption of CuO nanowires in the wavelength range 500−700 nm shall be due to free carrier absorption. The fitted curves match the experimental spectra well, elucidating the existence of the FCA mechanism in CuO thin films. The decay dynamics of $\Delta\alpha^{CuO}(\lambda,t)$ for the $^{24}C_{380}$ sample are best described by a triexponential decay function, and Figure 5c shows two representative $\Delta\alpha$ versus t curves at λ_b = 489 nm (the bleach dip) and λ_f = 749 nm (the high FCA).

Regardless of the wavelength, three time constants, T_1^{CuO} = 250 fs, T_2^{CuO} = 2.5 ps, and T_3^{CuO} > 150 ps, are obtained. These time constants are consistent with those reported by Othonos et al.[26] and Born et al.,[27] i.e., T_1^{CuO} is attributed to momentum relaxation via carrier−carrier scattering in the valence band, T_2^{CuO} is attributed to the carrier−phonon scattering within the valence band, and T_3^{CuO} is due to trapping and recombination. The EAS resulting from global analysis is shown in Figure 5d. A schematic summarizing these proposed relaxation processes is shown in Figure 6. The EAS for T_1^{CuO} captures the essential features for the TAS of the CuO film, manifests similarities to the $\Delta\alpha(\lambda,t=0)$. The EAS for T_3^{CuO} elucidates that a significant part of the free carriers in CuO has a very long lifetime. The fact that the $\Delta\alpha$ in Figure 5c does not decay to zero indicates that part of the free carriers lives for much longer than 150 ps. Both EAS for T_2^{CuO} and T_3^{CuO} show a bleach dip around λ_b = 475 nm, which corresponds to the depletion of electrons in the VB by the pump. It is also very interesting to notice how the wavelength λ_0 at EAS = 0 shifts with decay time. For T_1^{CuO}, λ_0 ~ 615 nm, which corresponds to 2.02 eV. This photon energy is close to the Urbach tail energy E_U^{CuO}, which defines the intrinsic absorbance edge of the material.[27,41] For T_2^{CuO}, λ_0 ~ 573 nm, which corresponds to 2.16 eV, close to the OBG

https://dx.doi.org/10.1021/acs.jpcc.0c08716
J. Phys. Chem. C 2020, 124, 24908−24918

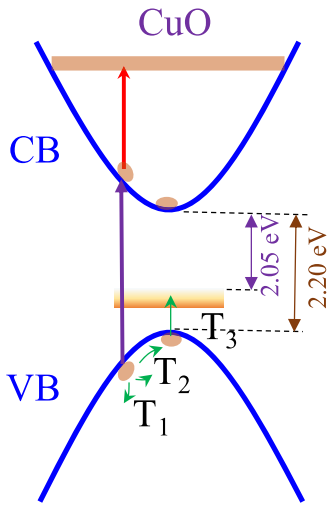

Figure 6. Proposed energy band structures and possible electron transition processes for the p-type CuO thin film.

(E_D^{CuO} = 2.20 eV) of our CuO sample; and for T_3^{CuO}, $\lambda_0 \sim 515$ nm (2.4 eV), close to the bleach dip location of $\Delta\alpha(\lambda,t = 0)$. By considering the EAS and the steady-state UV−VIS absorption spectrum shown in Figure 2a, it can be concluded that during the pumping the electrons in both the top of the VB and extended defect states are depleted, thus the absorption of probe light with $h\nu > E_U^{CuO}$ at a very short delay time T_1^{CuO} is minimized, i.e., a bleach occurs, while only the FCA at the conduction band occurs for $h\nu < E_U^{CuO}$. For $T_1^{CuO} < t < T_2^{CuO}$, the top of the band tail will be gradually filled with electrons so that additional absorption between the top of the band tail and the CB ($E_U^{CuO} < h\nu < E_D^{CuO}$) would be allowed, while for high-energy absorption ($h\nu > E_D^{CuO}$), the depletion still maintains. Finally, for $T_2^{CuO} < t < T_3^{CuO}$, the entire band tails (or the defect states) are partially filled with electrons, so that induced absorption with $h\nu < E_b^{CuO}$ would occur. Thus, most likely both the T_2^{CuO} and T_3^{CuO} are due to the defect state trapping.

3.5. TA Spectra of Cu_2O/CuO Thin Films. For a thin film with the mixed composition of Cu_2O and CuO, based on eq 4, it is expected that the overall signal is a sum of the contributions from both pure samples, i.e., the bleach due to saturation absorption of CuO and Cu_2O (eq 5), the induced absorption peak in Cu_2O (eq 6), and FCA in CuO (eq 7). Here, we assume that the effect of interfacial transition or charge separation has already been accounted for. Thus, from the spectroscopic point of view, the TAS for a mixed Cu_2O and CuO thin film should be dominated by at least four spectroscopic regions, the bleach regions of Cu_2O (450 < λ < 475 nm) and CuO (450 < λ < 650 nm), the resonant absorption region (475 < λ < 525 nm) due to defects of Cu_2O, and FAC region (λ > 650 nm) in CuO. The broad bleach region of CuO overlaps with the bleach and resonance absorption regions of Cu_2O, while the FCA region is solely governed by the amount of CuO in the sample. Also, due to the formation of Cu_2O/CuO heterojunction interfaces, new spectroscopic feature(s) is expected. Similarly, the carrier dynamics of the mixed films is determined by $T_1^{Cu_2O}$, T_1^{CuO}, T_2^{CuO}, the two long time constants, $T_2^{Cu_2O}$ and T_3^{CuO}, and possible time constant for charge separation.

To test above arguments, the samples $^{24}C_{150}$ (η_{Cu_2O} = 72%) and $^{2}C_{200}$ (η_{Cu_2O} = 29%) are taken as an example. Figure 7a shows some representative TA spectra $\Delta\alpha(\lambda,t)$ of sample $^{24}C_{150}$ at selective delay time, t = 0, 0.3, 0.8, 2.4, and 149 ps. At small time (t = 0 and 0.3 ps), the spectra in Figure 7a resemble the spectra in Figure 7b, i.e., a sharp bleach dip occurs at λ_b = 464 nm and a resonant absorption peak at λ_p = 498 nm. When t > 0.3 ps, both above spectral features are gone, and TA is dominated by a broad absorption (λ > 475 nm), and $\Delta\alpha(\lambda)$ increases slightly with λ, which is the characteristics for FCA. This time-dependent TAS behavior suggests that initially the carrier dynamics are dominated by Cu_2O, then when t > 0.3 ps, the dynamics are dominated by CuO. Note that for this sample, η_{Cu_2O} = 72%. This suggests that there is charge separation occurring between Cu_2O and CuO after 0.3 ps, and the electrons in the CB of Cu_2O could transition to the CB of CuO. The decay dynamics of $\Delta\alpha(\lambda,t)$ for the $^{24}C_{150}$ sample can be fitted by a triexponential decay function. Regardless of the wavelength, three time constants, T_1^{72} = 320 ± 50 fs, T_2^{72} = 2.9 ± 0.9 ps, and T_3^{72} = > 150 ps are obtained and the corresponding EAS is extracted, as shown in Figure 7b. Comparing the EAS features in Figure 7b with those shown in Figures 3d and 5d, and considering the corresponding lifetime, it is quite clear that the mechanism for T_1^{72} = 320 ± 50 fs resembles the dynamics of $T_1^{Cu_2O}$ = 293 fs; since the corresponding EASs share the same bleach and resonance absorption features, the T_1^{72} is dominated by hot electron dynamics in Cu_2O. In fact, since there is 72% of Cu_2O in the $^{24}C_{150}$ sample, it is understandable that the short time dynamics of the mixed-phase system is determined by Cu_2O.

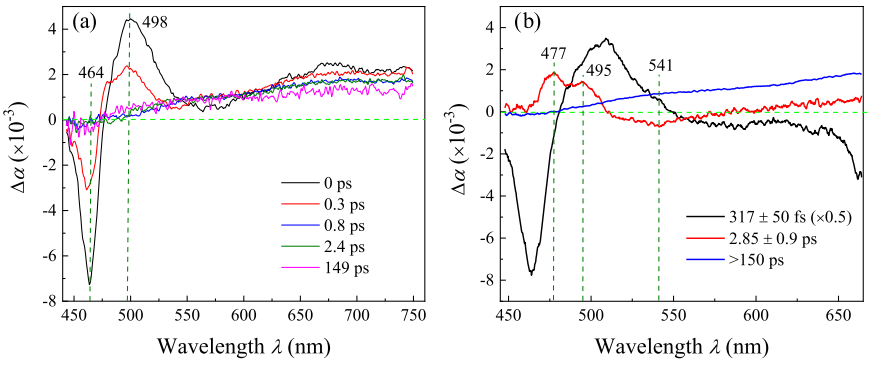

Figure 7. (a) Representative chirp-corrected TA spectra of sample $^{24}C_{150}$ (η_{Cu_2O} = 72%) at delay time t = 0, 0.3, 0.8, 2.4, and 150 ps, respectively, and (b) plots of the corresponding evolution associated spectra based on a triexponential decay analysis.

https://dx.doi.org/10.1021/acs.jpcc.0c08716
J. Phys. Chem. C 2020, 124, 24908−24918

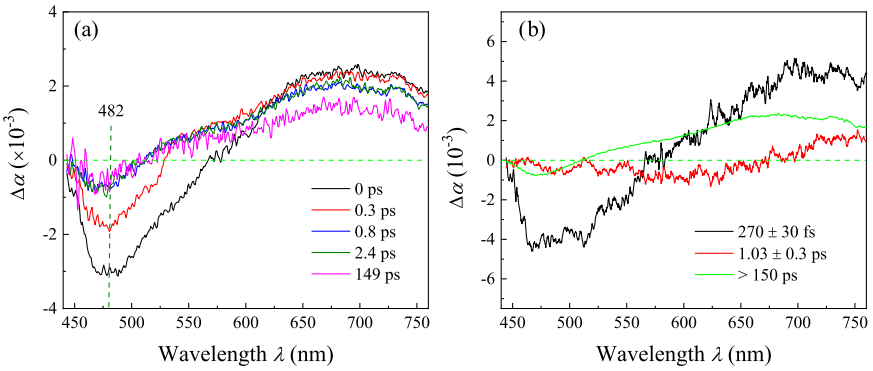

Figure 8. (a) Representative chirp-corrected TA spectra of sample $^{2}C_{200}$ (η_{Cu_2O} = 29%) at delay time t = 0, 0.3, 0.8, 2.4, and 150 ps and (b) plots of the corresponding evolution associated spectra based on a triexponential decay analysis.

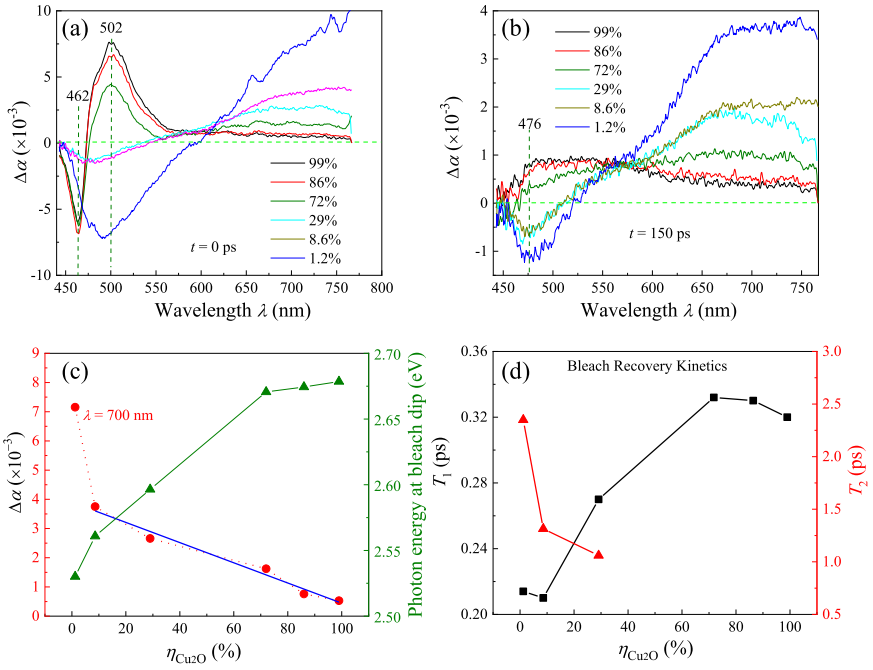

Figure 9. Change of TA spectra for different Cu_2O/CuO thin film samples at (a) t = 0 ps and (b) t = 150 ps. (c) Plots of the photonic energy of the bleach dip and the $\Delta\alpha$ (λ = 700 nm, t = 0 ps) versus η_{Cu_2O}. (d) Plots of T_1 and T_2 versus η_{Cu_2O}.

However, the long-time carrier dynamics, T_3^{72} > 150 ps, is governed by CuO. The EAS for T_3^{72} is very similar to that of T_3^{CuO}, both EAS increases monotonically with the wavelength λ, except that there is a weak bleach observed in the wavelength range of 450−500 nm for CuO. Also $\Delta\alpha(\lambda,t)$ in Cu_2O is almost fully recovered in t < 2 ps (see Figure 3c), while for CuO, $\Delta\alpha(\lambda,t)$ still maintains a relative high value even after 10 ps, which indicates a longer trapping lifetime. The EAS for T_2^{72} = 2.9 ± 0.9 ps does not resemble any of the EAS for Cu_2O and CuO and is considered to be the result of new charge dynamics. By carefully examining this EAS, there exist two resonance absorption peaks, one at λ = 477 nm (2.60 eV) and the other at λ = 495 nm (2.50 eV). These two resonance absorption peaks cannot be generated by the charge-transfer mechanism since only one resonance mechanism in Cu_2O is possible. Notice that the resonant energies for these two peaks are both larger than that (2.46 eV) observed in Cu_2O, which indicates that these could be two new shallow acceptor states, 0.08 eV and 0.18 eV above the VB, induced in Cu_2O during oxidation, compared to the original acceptor states, which is 0.22 eV above the VB. The different dynamics are possible due to the following reasons: first, comparing the static absorption spectra $\alpha(h\nu)$ for samples $^{24}C_{150}$ and $^{2}C_{150}$ as shown in Figure S8, there is significantly more absorption for the $^{24}C_{150}$ sample at the band tail; second, the formation of the sample $^{24}C_{150}$ from $^{2}C_{150}$ is an oxidation process. This process is usually a diffusion-limited reaction, which means that there is no abrupt change in the interfaces between Cu_2O and CuO. In fact, between the pure Cu_2O and CuO phases, there is a diffusion zone that composes of a gradient composition of Cu_xO, where 1 < x < 2. So, in this diffusion zone, there is a deficiency of Cu^+ in Cu_2O, which can generate extra shallow donor states. In addition, the sample $^{24}C_{150}$ still has Cu_2O and CuO interfaces and charge separation could occur as discussed above. The existence of a mixed interface of Cu_2O and CuO indicated that there could be interfacial defect states generated. Therefore, in the $^{24}C_{150}$ sample with 72% of Cu_2O, the short time dynamics T_2^{72} could be governed by the trapping of the shallow donor states in Cu_2O or the charge separation process at the Cu_2O and CuO interfaces. The two resonance

https://dx.doi.org/10.1021/acs.jpcc.0c08716
J. Phys. Chem. C 2020, 124, 24908−24918

absorption peaks, one at λ = 477 and 495 nm, could be due to these defect states.

Figure 8a shows some representative TA spectra $\Delta\alpha(\lambda,t)$ of sample $^{2}C_{200}$, and the spectral features and time-dependent behaviors are similar to that of the $^{24}C_{380}$ sample, i.e., a broad bleach dip occurs at λ_b = 492 nm, which is slightly blue shifted compared to that of the λ_b = 498 nm for the $^{24}C_{380}$ sample. Such a blue shift in λ_b is attributed to the presence of Cu_2O in the film. Also, a broad absorption bump centered around λ_f = 700 nm occurs and is assigned to FCA. With an increase in delay time t, the overall spectral features remain unchanged, while the amplitudes keep on decreasing. Compared to spectra shown in Figure 5b, the amplitudes for bleach and FCA are significantly reduced, which should be due to the absorption from Cu_2O. Considering the energy structure of CuO/Cu_2O heterostructure, there could be hole injection from the VB of CuO to the VB of Cu_2O, reducing the overall TAS amplitude. The decay dynamics of $\Delta\alpha(\lambda,t)$ for the sample $^{2}C_{200}$ also follows a triexponential decay with T_1^{29} = 270 ± 50 fs, T_2^{29} = 1.03 ± 0.3 ps, and T_3^{29} > 150 ps. The corresponding EAS shown in Figure 8b are very similar to those shown in Figure 5d of the $^{24}C_{380}$ sample. Compared to the corresponding lifetime, it is quite clear that the mechanism for T_1^{29} = 270 ± 50 fs resembles the dynamics of T_1^{CuO} = 250 ± 20 fs, which is dominated by carrier−carrier scattering or thermalization in CuO; T_3^{29} > 150 ps is also assigned to trapping by defects, similar to the $^{24}C_{380}$ sample. The fact that T_2^{29} is much smaller than T_2^{CuO} suggests that more defect states close to VB of CuO such as interfacial states, copper ion centers, etc. are produced due to the presence of Cu_2O.

To gain a systematic understanding on how ηCu_2O affects the carrier dynamics of the mixed-phase Cu_2O/CuO thin films, we performed TAS on the samples listed in Table 1. Figure 9a,b shows the TA spectra of different samples at t = 0 and 150 ps, both showing strong variations in TA spectra with η_{Cu_2O}. At t = 0 ps, $\Delta\alpha(\lambda)$ is very sensitive to the minute amount of Cu_2O added in CuO thin films. When η_{Cu_2O} increases from 1.2 to 8.6%, the bleach dip amplitude decreases significantly from 7.2 × 10^{-3} (λ = 491 nm) to 1.4 × 10^{-3} (λ = 482 nm), while the FCA decreases from 1.0 × 10^{-2} to 4.1 × 10^{-3} at λ = 762 nm. When η_{Cu_2O} further increases to 29%, the overall spectra features change slightly. For these three samples, similar TAS features like that of the pure CuO thin film ($^{24}C_{380}$). The η_{Cu_2O} = 72% sample starts to show the bleach and resonance absorption features similar to those of the pure Cu_2O thin film. With a further increase in η_{Cu_2O}, both features become more prominent. However, at longer delay time, the TAS features and their change with η_{Cu_2O} become significantly different. The spectra for CuO-dominated samples (η_{Cu_2O} = 1.2, 8.6, and 29%) show narrow banded bleach dips centered around λ_b = 476 nm (2.60 eV), while a broad band FCA is observed for λ > 525 nm. The TAS for Cu_2O-dominated samples (η_{Cu_2O} = 72, 86, and 99%) all show broad absorption features maximized around λ > 476 nm. The significant difference in short time TAS for different η_{Cu_2O} demonstrates that the fast dynamics depends closely on the composition, while the similarity in long time TAS illustrates that the long life carrier dynamic mechanism is similar.

In addition, according to the discussions above, the bleach dip wavelength reflects the effective bandgap of the materials. According to Figure 2b, the effective optical bandgap increases monotonically with η_{Cu_2O}. So, a similar trend is expected for the dip wavelength. Figure 9c plots the photonic energy associated with the bleach dip as a function of η_{Cu_2O}, and the energy increases monotonically with η_{Cu_2O}, which is consistent with Figure 2b. In addition, the $\Delta\alpha(\lambda)$ in the longer-wavelength region corresponds to FCA and based on eqs 4 and 7, the $\Delta\alpha(\lambda)$ at longer λ is a linear function of η_{Cu_2O}. Figure 9c also plots the $\Delta\alpha(\lambda)$ at λ > 700 nm versus η_{Cu_2O}. Except for the last data point at η_{Cu_2O} = 1.2%, all other data follow a linear relationship very well.

The lifetimes for the bleach recovery kinetics of the samples were extracted by a double exponential decay model for samples with η_{Cu_2O} = 86 and 99% and a triple exponential decay model for other samples. Figure 9d summarizes both T_1 and T_2 as a function of η_{Cu_2O}. As discussed for CuO, T_1 is due to carrier−carrier scattering or thermalization. As shown in Figure 9d, when $\eta_{Cu_2O} \leq$ 72%, T_1 increases monotonically with η_{Cu_2O}; when η_{Cu_2O} > 72%, T_1 decreases slightly with η_{Cu_2O}. When η_{Cu_2O} = 72%, T_1 reaches a maximum. Thus, if the photocatalytic performance of the Cu_2O/CuO is dominated by the hot electrons, these results suggest that the η_{Cu_2O} = 72% sample, i.e., the $^{24}C_{150}$, is the optimized sample. This prediction is consistent with previous experimental results by Basnet et al., where the dye photodecay rates of mixed-phase CuO/Cu_2O nanorod thin films prepared by a similar method were studied systematically.[34] Figure 4 in ref 34 indicates that both the photoreduction and photooxidation rates are relatively high at η_{Cu_2O} = 72%.[34] The lifetime T_2 is caused by carrier−phonon scattering process in the VB in CuO. The decrease of T_2 when η_{Cu_2O} increases from 1.2 to 30% shown in Figure 9d could be due to the fact that during the transition from CuO to Cu_2O, and the formation of the CuO/Cu_2O interfaces, less carrier−phonon scattering process would occur in the mixed material.

4. CONCLUSIONS

In summary, we systematically fabricated the Cu_2O, CuO, and mixed-phase Cu_2O/CuO thin films with different relative compositions by oxidizing Cu films at a temperature from 150 to 380 °C for a time period of 2−24 h. The XRD characterizations show that the Cu_2O composition in these films can vary from 1.2 to 99%, while the corresponding CuO composition changes from 98.8 to 1%. Since these films are prepared under similar conditions, they can serve as excellent model samples to understand how the relative composition of Cu_2O/CuO plays a role in photoinduced carrier dynamics by ultrafast transient absorption spectroscopy. Detailed studies show that the absorption dynamics of a pure p-type Cu_2O thin film follows a biexponential decay, with a fast time ∼0.3 ps and a long time constant >150 ps. Based on the spectroscopic features, energy band structures, and possible electron transition process, rate equations for the electron dynamics have been established. The short time constant is attributed to the relaxation of hot electrons by scattering or thermalization, while the long time constant could be due to the defect trapping. For the pure p-type CuO sample, the TAS is dominated by a bleach dip and free carrier absorption. Its triexponential decay dynamics result in three time constants, 0.25, 2.5, and >150 ps, which correspond to carrier−carrier

https://dx.doi.org/10.1021/acs.jpcc.0c08716
J. Phys. Chem. C 2020, 124, 24908−24918

scattering or thermalization, defect trapping, and interband transition. For the mixed-phased Cu_2O/CuO thin films, if Cu_2O dominates the composition, the very short time dynamics (<1 ps) are dominated by Cu_2O while the long time behavior (>150 ps) is determined by CuO. The charge separation or other interfacial defect determines the carrier dynamics in a few pico-second. If CuO dominates the composition, the carrier dynamics are led by the CuO, and a photo leach and free carrier absorption dictate the TAS. In fact, it is discovered that both the bleach photon energy, the short and medium time constants are a function of the Cu_2O composition. This study shows that for the Cu_2O/CuO heterostructures, there is charge separation that could significantly change the carrier lifetime in pico-second time scale. Depending on the composition and how the interface is formed, processes like electron migration from Cu_2O to CuO, or hole injection from CuO to Cu_2O, or defect state absorption could change the lifetimes of the photoinduced carriers. For the thin-film samples prepared by oxidation, it is found that for Cu_2O composition of 72%, the hot electrons' lifetime (T_1) reaches a maximum, which suggests that this film could maximize the photocatalytic performance.

■ ASSOCIATED CONTENT

Supporting Information

The Supporting Information is available free of charge at https://pubs.acs.org/doi/10.1021/acs.jpcc.0c08716.

Photos of different samples, the effect of the reflection spectra on the determination of absorption spectra, Tauc plots, optical bandgap estimation, the explanation of global analysis of transient absorption data, the comparison of TA spectra and the UV−vis derivative spectra of CuO and Cu_2O thin films, the free carrier absorption fitting results for CuO thin film, and the comparison of the extinction spectra of samples $^{24}C_{150}$ and $^{2}C_{150}$ (PDF)

■ AUTHOR INFORMATION

Corresponding Authors

Yiping Zhao − *Department of Physics and Astronomy, University of Georgia, Athens, Georgia 30605, United States;* orcid.org/0000-0002-3710-4159; Email: zhaoy@uga.edu

Susanne Ullrich − *Department of Physics and Astronomy, University of Georgia, Athens, Georgia 30605, United States;* orcid.org/0000-0002-1828-2777; Email: ullrich@uga.edu

Authors

Learnmore Shenje − *Department of Physics and Astronomy, University of Georgia, Athens, Georgia 30605, United States*

Steven Larson − *Department of Physics and Astronomy, University of Georgia, Athens, Georgia 30605, United States;* orcid.org/0000-0003-4681-0749

Complete contact information is available at: https://pubs.acs.org/10.1021/acs.jpcc.0c08716

Notes

The authors declare no competing financial interest.

■ ACKNOWLEDGMENTS

This work, L.S., and S.U. were supported by the National Science Foundation grant CHE-1362237 and CHE-1800050. S.L. and Y.Z. were supported by the National Science Foundation (ECCS-1609815 and ECCS-1808271).

■ REFERENCES

(1) Khojier, K.; Savaloni, H.; Sadeghi, Z. A Comparative Investigation on Growth, Nanostructure and Electrical Properties of Copper Oxide Thin Films as a Function of Annealing Conditions. *J. Theor. Appl. Phys.* **2014**, *8*, 116.

(2) Sanal, K.; Vikas, L.; Jayaraj, M. Room Temperature Deposited Transparent P-Channel CuO Thin Film Transistors. *Appl. Surf. Sci.* **2014**, *297*, 153−157.

(3) Brown, K. E. R.; Choi, K. S. Electrochemical Synthesis and Characterization of Transparent Nanocrystalline Cu_2O Films and Their Conversion to CuO Films. *Chem. Commun.* **2006**, 3311−3313.

(4) Wang, P.; Zhao, X.; Li, B. ZnO-Coated CuO Nanowire Arrays: Fabrications, Optoelectronic Properties, and Photovoltaic Applications. *J. Opt. Express* **2011**, *19*, 11271−11279.

(5) Born, B.; Geoffroy-Gagnon, S.; Krupa, J. D.; Hristovski, I. R.; Collier, C. M.; Holzman, J. F. Ultrafast All-Optical Switching Via Subdiffractional Photonic Nanojets and Select Semiconductor Nanoparticles. *ACS Photonics* **2016**, *3*, 1095−1101.

(6) Johan, M. R.; Suan, M. S. M.; Hawari, N. L.; Ching, H. A. Annealing Effects on the Properties of Copper Oxide Thin Films Prepared by Chemical Deposition. *Int. J. Electrochem. Sci* **2011**, *6*, 6094−6104.

(7) Wang, S. L.; Li, P. G.; Zhu, H. W.; Tang, W. H. Controllable Synthesis and Photocatalytic Property of Uniform CuO/Cu_2O Composite Hollow Microspheres. *Powder Technol.* **2012**, *230*, 48−53.

(8) Wu, H.-W.; Lee, S.-Y.; Lu, W. C.; Chang, K. S. Piezoresistive Effects Enhanced the Photocatalytic Properties of Cu_2O/CuO Nanorods. *Appl. Surf. Sci.* **2015**, *344*, 236−241.

(9) Peng, F.; Sun, Y.; Yu, W.; Lu, Y.; Hao, J.; Cong, R.; Shi, J.; Ge, M.; Dai, N. Gas Sensing Performance and Mechanism of CuO(P)-WO_3(N) Composites to H_2S Gas. *Nanomaterials* **2020**, *10*, 1162.

(10) Yang, Y.; Yang, J.; Yin, W.; Huang, F.; Cui, A.; Zhang, D.; Li, W.; Hu, Z.; Chu, J. Annealing Time Modulated the Film Microstructures and Electrical Properties of P-Type CuO Field Effect Transistors. *Appl. Surf. Sci.* **2019**, *481*, 632−636.

(11) Kumar, V.; Masudy-Panah, S.; Tan, C. C.; Wong, T. K. S.; Chi, D. Z.; Dalapati, G. K. In *Copper Oxide Based Low Cost Thin Film Solar Cells*, 2013 IEEE 5th International Nanoelectronics Conference (INEC), Singapore, 2−4 Jan 2013; pp 443−445.

(12) Zhu, Y.; Xu, Z.; Yan, K.; Zhao, H.; Zhang, J. One-Step Synthesis of CuO−Cu_2O Heterojunction by Flame Spray Pyrolysis for Cathodic Photoelectrochemical Sensing of L-Cysteine. *ACS Appl. Mater. Interfaces* **2017**, *9*, 40452−40460.

(13) Dubale, A. A.; Tamirat, A. G.; Chen, H. M.; Berhe, T. A.; Pan, C. J.; Su, W. N.; Hwang, B. J. A Highly Stable CuS and CuS−Pt Modified Cu_2O/CuO Heterostructure as an Efficient Photocathode for the Hydrogen Evolution Reaction. *J. Mater. Chem. A* **2016**, *4*, 2205−2216.

(14) Liu, X.; Chen, J.; Liu, P.; Zhang, H.; Li, G.; An, T.; Zhao, H. Controlled Growth of CuO/Cu_2O Hollow Microsphere Composites as Efficient Visible-Light-Active Photocatalysts. *Appl. Catal., A* **2016**, *521*, 34−41.

(15) Jiang, D.; Xue, J.; Wu, L.; Zhou, W.; Zhang, Y.; Li, X. Photocatalytic Performance Enhancement of CuO/Cu_2O Heterostructures for Photodegradation of Organic Dyes: Effects of CuO Morphology. *Appl. Catal., B* **2017**, *211*, 199−204.

(16) Yang, Y.; Xu, D.; Wu, Q.; Diao, P. Cu_2O/CuO Bilayered Composite as a High-Efficiency Photocathode for Photoelectrochemical Hydrogen Evolution Reaction. *Sci. Rep.* **2016**, *6*, No. 35158.

(17) Shah, J. *Ultrafast Spectroscopy of Semiconductors and Semiconductor Nanostructures*; Springer Science & Business Media, 2013; Vol. *115*, pp 74−75.

(18) Zhang, J. Z. Interfacial Charge Carrier Dynamics of Colloidal Semiconductor Nanoparticles. *J. Phys. Chem. B* **2000**, 7239−7253.

(19) Othonos, A. Probing Ultrafast Carrier and Phonon Dynamics in Semiconductors. *J. Appl. Phys.* **1998**, *83*, 1789−1830.

(20) Yoshihara, T.; Katoh, R.; Furube, A.; Tamaki, Y.; Murai, M.; Hara, K.; Murata, S.; Arakawa, H.; Tachiya, M. Identification of Reactive Species in Photoexcited Nanocrystalline TiO_2 Films by Wide-Wavelength-Range (400−2500 nm) Transient Absorption Spectroscopy. *J. Phys. Chem. B* **2004**, *108*, 3817−3823.
(21) Willis, R. L.; Olson, C.; O'Regan, B.; Lutz, T.; Nelson, J.; Durrant, J. R. Electron Dynamics in Nanocrystalline ZnO and TiO_2 Films Probed by Potential Step Chronoamperometry and Transient Absorption Spectroscopy. *J. Phys. Chem. B* **2002**, *106*, 7605−7613.
(22) Tamaki, Y.; Furube, A.; Katoh, R.; Murai, M.; Hara, K.; Arakawa, H.; Tachiya, M. Trapping Dynamics of Electrons and Holes in a Nanocrystalline TiO_2 Film Revealed by Femtosecond Visible/near-Infrared Transient Absorption Spectroscopy. *C. R. Chim.* **2006**, *9*, 268−274.
(23) Cherepy, N. J.; Liston, D. B.; Lovejoy, J. A.; Deng, H.; Zhang, J. Z. Ultrafast Studies of Photoexcited Electron Dynamics in Γ- and A-Fe_2O_3 Semiconductor Nanoparticles. *J. Phys. Chem. B* **1998**, *102*, 770−776.
(24) Barroso, M.; Mesa, C. A.; Pendlebury, S. R.; Cowan, A. J.; Hisatomi, T.; Sivula, K.; Grätzel, M.; Klug, D. R.; Durrant, J. R. Dynamics of Photogenerated Holes in Surface Modified A-Fe_2O_3; Photoanodes for Solar Water Splitting. *Proc. Natl. Acad. Sci. U.S.A.* **2012**, *109*, 15640.
(25) Bauer, C.; Boschloo, G.; Mukhtar, E.; Hagfeldt, A. Ultrafast Relaxation Dynamics of Charge Carriers Relaxation in ZnO Nanocrystalline Thin Films. *Chem. Phys. Lett.* **2004**, *387*, 176−181.
(26) Othonos, A.; Zervos, M. Ultrafast Hole Carrier Relaxation Dynamics in P-Type CuO Nanowires. *Nanoscale Res. Lett.* **2011**, *6*, 622.
(27) Born, B.; Krupa, J. D.; Geoffroy-Gagnon, S.; Hristovski, I. R.; Collier, C. M.; Holzman, J. Ultrafast Charge-Carrier Dynamics of Copper Oxide Nanocrystals. *ACS Photonics* **2016**, *3*, 2475−2481.
(28) Azimi, H.; Kuhri, S.; Osvet, A.; Matt, G.; Khanzada, L. S.; Lemmer, M.; Luechinger, N. A.; Larsson, L. I.; Zeira, E.; et al. Effective Ligand Passivation of Cu_2O Nanoparticles through Solid-State Treatment with Mercaptopropionic Acid. *J. Am. Chem. Soc.* **2014**, *136*, 7233−7236.
(29) Paracchino, A.; Brauer, J. C.; Moser, J. E.; Thimsen, E.; Graetzel, M. Synthesis and Characterization of High-Photoactivity Electrodeposited Cu_2O Solar Absorber by Photoelectrochemistry and Ultrafast Spectroscopy. *J. Phys. Chem. C* **2012**, *116*, 7341−7350.
(30) Tanimura, H.; Tanimura, K.; van Loosdrecht, P. H. M. Dynamics of Incoherent Exciton Formation in Cu_2O: Time- and Angle-Resolved Photoemission Spectroscopy. *Phys. Rev. B* **2019**, *100*, No. 115204.
(31) Borgwardt, M.; Omelchenko, S. T.; Favaro, M.; Plate, P.; Höhn, C.; Abou-Ras, D.; Schwarzburg, K.; Van De Krol, R.; Atwater, H. A.; Lewis, N. S.; et al. Femtosecond Time-Resolved Two-Photon Photoemission Studies of Ultrafast Carrier Relaxation in Cu_2O Photoelectrodes. *Nat. Commun.* **2019**, *10*, No. 2106.
(32) Khojier, K.; Savaloni, H.; Sadeghi, Z. A Comparative Investigation on Growth, Nanostructure and Electrical Properties of Copper Oxide Thin Films as a Function of Annealing Conditions. *J. Theor. Appl. Phys.* **2014**, *8*, 116.
(33) Park, J. H.; Natesan, K. Oxidation of Copper and Electronic Transport in Copper Oxides. *Oxid. Met.* **1993**, *39*, 411−435.
(34) Basnet, P.; Zhao, Y. Tuning the Cu_xO Nanorod Composition for Efficient Visible Light Induced Photocatalysis. *Catal. Sci. Technol.* **2016**, *6*, 2228−2238.
(35) Hastings, G.; Makita, H.; Shenje, L. T.; Ullrich, S. Femtosecond Time-Resolved Spectroscopy for the Study of Photosystem I Reaction Centers at 77 K. *Front. Sci. Technol. Eng. Math.* **2019**, *3*, 63−70.
(36) Snellenburg, J. J.; Laptenok, S. P.; Seger, R.; Mullen, K. M.; Van Stokkum, I. H. M. Glotaran: A Java-Based Graphical User Interface for the R-Package Timp. *J. Stat. Software* **2012**, *49*, 1−22.
(37) *Surface Xplorer*, version 4.2.0; Ultrafast System: Sarasota, FL, 2019.
(38) Köferstein, R. Synthesis, Phase Evolution and Properties of Phase-Pure Nanocrystalline $BiFeO_3$ Prepared by a Starch-Based Combustion Method. *J. Alloys Compd.* **2014**, *590*, 324−330.
(39) Rodríguez-Carvajal, J. Recent Advances in Magnetic Structure Determination by Neutron Powder Diffraction. *Phys. B* **1993**, *192*, 55−69.
(40) Viezbicke, B. D.; Patel, S.; Davis, B. E.; Birnie, D. P., III Evaluation of the Tauc Method for Optical Absorption Edge Determination: ZnO Thin Films as a Model System. *Phys. Status Solidi B* **2015**, *252*, No. 1700.
(41) Lamri Zeggar, M.; Messaoudi, M.; Aida, M. S.; Attaf, N. Gap States Density Measurement in Copper Oxide Thin Films. *Mater. Sci. Semicond. Process.* **2016**, *45*, 32−35.
(42) Zervos, M.; Othonos, A.; Sergides, M.; Pavloudis, T.; Kioseoglou, J. Observation of the Direct Energy Band Gaps of Defect-Tolerant Cu_3N by Ultrafast Pump-Probe Spectroscopy. *J. Phys. Chem. C* **2020**, *124*, 3459−3469.
(43) Meyer, B. K.; Polity, A.; Reppin, D.; Becker, M.; Hering, P.; Klar, P. J.; Sander, T.; Reindl, C.; Benz, J.; Eickhoff, M.; et al. Binary Copper Oxide Semiconductors: From Materials Towards Devices. *Phys. Status Solidi B* **2012**, *249*, 1487−1509.
(44) Heinemann, M.; Eifert, B.; Heiliger, C. Band Structure and Phase Stability of the Copper Oxides Cu_2O, CuO, and Cu_4O_3. *Phys. Rev. B* **2013**, *87*, No. 115111.
(45) Wheeler, D. A.; Zhang, J. Z. Exciton Dynamics in Semiconductor Nanocrystals. *Adv. Mater.* **2013**, *25*, 2878−2896.
(46) De Laurentis, M.; Irace, A. Optical Measurement Techniques of Recombination Lifetime Based on the Free Carriers Absorption Effect. *J. Solid State Phys.* **2014**, No. 291469.
(47) Pankove, J. I. *Optical Processes in Semiconductors*; Courier Corporation, 1975.
(48) Wang, W. N.; Wu, F.; Myung, Y.; Niedzwiedzki, D. M.; Im, H. S.; Park, J.; Banerjee, P.; Biswas, P. Surface Engineered CuO Nanowires with ZnO Islands for CO_2 Photoreduction. *ACS Appl. Mater. Interfaces* **2015**, *7*, 5685−5692.

https://dx.doi.org/10.1021/acs.jpcc.0c08716
J. Phys. Chem. C 2020, 124, 24908−24918